ICAS 2021 SHANG HAI
International Council of the Aeronautical Sciences
32nd Congress of the International Council of the Aeronautical Sciences
September 6-10, 2021 Pudong Shangri-La, Shanghai, China

VALIDATION OF A DISCONTINUOUS GALERKIN BASED DES SOLVER IN FLOW PROBLEMS USING HIGH PERFORMANCE COMPUTING

I. Bosnyakov, S. Bosnyakov, S. Mikhaylov, V. Podaruev, A. Troshin & A. Wolkov

Central Aerohydrodynamic Institute (TsAGI), Zhukovsky, Moscow region, 140180, Russia

Abstract

Validation of Discontinuous Galerkin method designed for unsteady computations is presented. Explicit 4th order 5-stage strong stability-preserving Runge–Kutta scheme is used in conjunction with global time stepping. Shape functions are orthonormal polynomials in physical space of order K of up to 5, formally giving a K + 1 accuracy order of the scheme. Bassi & Rebay 2 approximation of viscous fluxes is adopted. Implicit Large Eddy Simulation technique (ILES) is used as well as Delayed Detached Eddy Simulation (DDES, 2006) with an option of employing the wall functions. Test cases used for validation are Taylor–Green vortex, NASA axisymmetric jet, and periodic hill flow. The results include accuracy vs. computational cost comparisons and scalability assessment on up to 50 000 CPU cores.

Keywords: Discontinuous Galerkin method, High-Order, ILES, DDES, Taylor–Green vortex, periodic hill flow, axisymmetric jet.

1. Introduction

Discontinuous Galerkin (DG) method is considered to be one of the most promising high-order methods (HOM) for large eddy simulations in industrial aerodynamic problems. It is easily implemented in the case of unstructured meshes suitable to approximate complex geometries and is resistant to weaknesses in mesh quality. It can be easy implemented for parallel computer systems with large number of cores due to the compact stencil consisting only the nearest cell neighbours. High order may be achieved on smooth solutions using appropriate base functions. Its finite element nature matches well with finite volume properties. For example, like in Godunov scheme, DG method takes into account the direction of disturbance propagation when approximating the fluxes through the interfaces between the cells. It allows to obtain stable solution without adding artifitial viscosity to the equations.

In this paper we present the current level of the technology development in Central Aerohydrodynamic Institute (TsAGI, Russia). It is worth mentioning that TsAGI in-house code EWT has been developed since 1996 for different types of problems and DG solver was implemented to make code more flexible for practical simulations. Now it is focused on simulating the unsteady aerodynamics of turbulent flows, among other areas. Available base allowed TsAGI to take part in European H2020 project TILDA (“Towards Industrial LES/DNS in Aeronautics”, reference number 635962) and obtain new results which are presented in this paper.

The structure of the paper is as follows. In section 2, equation system is presented and formulation of the numerical scheme is described. Special attention is paid to the balance between accuracy and code efficiency. In section 3, the test cases selected in TILDA project are studied, such as Taylor-Green Vortex (from DLR), Periodic Hill Flow (from ERCOFTAC) and NASA axisymmetric jet. Also, the problem of code efficiency is considered in details. As an example, scalability test is performed on HPC cluster containing 50,000 CPU cores. Efficiency of the algorithm is disscussed together with quality of results. Final conclusions in section 4 summarize the results of this research.

2. Numerical Method

2.1 Equation System

Navier–Stokes equation system describing a gas flow in the domain D is written in conservative form,

$$\frac{\partial \mathrm{U}}{\partial t} + \nabla \cdot \mathbf{F}(\mathrm{U}, \mathbf{G}) = 0\,, \qquad (1)$$

where $U = \left(\rho, \rho u, \rho v, \rho w, \rho E\right)^{\mathrm{T}}$ is conservative variable vector, $\mathbf{F}$ is mass, momentum and energy flux vector, and $\mathbf{G} = \nabla \mathrm{U}$ is gradient vector. Specific total energy E is defined as

$$E = \frac{u^2 + v^2 + w^2}{2} + \frac{RT}{\gamma - 1}\,,$$

where $R = 287.065\ \mathrm{J/(kg \cdot K)}$ is air gas constant and $\gamma = 1.4$ is adiabatic exponent. Perfect gas equation of state is used, $p = \rho RT$ .Flux vector is splitted into two terms corresponding to different physical processes: $\mathbf{F} = \mathbf{F}^{conv} + \mathbf{F}^{diff}$. Convective fluxes along a coordinate axis k are given by a formula

$$F_k^{conv} = \left(\rho u_k\,,\ \rho u u_k + p\delta_{xk}\,,\ \rho v u_k + p\delta_{yk}\,,\ \rho w u_k + p\delta_{zk}\,,\ \rho E u_k + p u_k\right)^{\mathrm{T}}.$$

Diffusive fluxes due to molecular viscosity action are

$$F_k^{diff} = \left(0,\ \tau_{xk}\,,\ \tau_{yk}\,,\ \tau_{zk}\,,\ \tau_{xk}u + \tau_{yk}v + \tau_{zk}w + q_k\right)^{\mathrm{T}}.$$

Momentum and energy molecular fluxes are defined as

$$\tau_{ij} = -\left(\mu + \mu_T\right)\left(\frac{\partial u_i}{\partial x_j} + \frac{\partial u_j}{\partial x_i} - \frac{2}{3} div\mathbf{V}\ \delta_{ij}\right), \quad q_k = -\frac{\mu C_p}{\mathrm{Pr}}\frac{\partial T}{\partial x_k}\,.$$

Viscosity coefficient is supposed to be constant, $\mu = 1.72 \cdot 10^{-5}\ \mathrm{kg/(m \cdot s)}$. Prandtl number Pr is taken to be 0.71 while specific heat capacity C_p is $\gamma R/(\gamma - 1)$.

Navier-Stokes equation system is used for Direct Numerical Simulations (DNS) of turbulent flows and for underresolved Implicit Large Eddy Simulations (ILES). The latter case corresponds to zero value of subgrid viscosity, $\mu_T = 0$. If a Delayed Detached Eddy Simulation [7] is to be used instead, the hybrid eddy/subgrid viscosity is determined from an additional equation in the equation system.

A discretized counterpart of (1) is solved in a domain D_h . It approximates the equations with accuracy order D_h . The domain is divided into N_e non-overlapping elements,

$$D_h = \bigcup_{i=1}^{N_e} \Omega_i\,.$$

In the present paper, two types of elements are used, namely “linear” and “quadratic” hexahedrons. A “linear” hexahedron is defined by the coordinates of its 8 vertices, see Fig. 1, a. Using these coordinates, a serendipity transformation [1] of a standard cube $[-1,1]\times[-1,1]\times[-1,1]$ into the hexahedron may be formed,

$$x = x(\xi, \eta, \zeta), \quad y = y(\xi, \eta, \zeta), \quad z = z(\xi, \eta, \zeta).$$

In physical space, the faces and edges of the hexahedron are supposed to be the maps of the corresponding faces and edges of a standard cube.

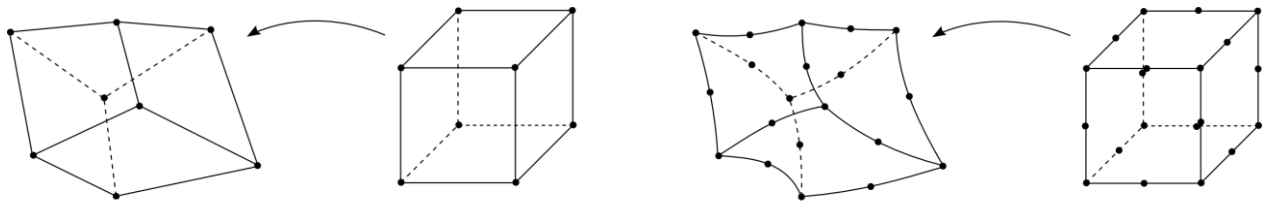

a) **b)**

Figure 1. Elementary hexahedrons and their mappings: a) "linear", b) "quadratic"

A "quadratic" hexahedron is defined by 20 points, see Fig. 1, b. In addition to 8 vertices, coordinates of the centers of its 12 edges are used. The edges of a "linear" element are straight line segments while the edges of "quadratic" element are parabolic curves.
Serendipity transformations are polynomials. They are used to distribute the Gauss points and their weights in the volumes of the elements and on their faces, and also to determine normal vectors to the faces. In DG solution, in each element Ω_i is approximated by an expansion over basis functions. Let us expand the conservative variables as follows:

$$\mathrm{U}(\mathbf{x}, t) = \sum_{j=1}^{K_f} \mathrm{u}_j(t)\,\varphi_j(\mathbf{x})\,. \tag{2}$$

After this discretization, expansion coefficients u_j become the main unknown values of the method. Let us take $\varphi_j(\mathbf{x})$ functions, $j = 1, \ldots, K_f$, to be the polynomial basis with elements of degree up to K in physical space, which is expected to provide accuracy order $(K+1)$ for smooth flow fields. In this case, the number of basis functions K_f is related to K by the formula $K_f = (K+1)(K+2)(K+3)/6$. Following the approach developed in Ref. 11, let us form an orthogonal and normalized basis function set. At the first step, we determine the barycenter coordinates of Ω_i element:

$$x_0 = \frac{\int_\Omega x\,d\Omega}{\int_\Omega d\Omega}, \quad y_0 = \frac{\int_\Omega y\,d\Omega}{\int_\Omega d\Omega}, \quad z_0 = \frac{\int_\Omega z\,d\Omega}{\int_\Omega d\Omega}.$$

After that, we calculate the components of inertia tensor of Ω_i:

$$\mathbf{I} = \begin{bmatrix} \int_\Omega \left(\tilde{y}^2 + \tilde{z}^2\right) d\Omega & -\int_\Omega \tilde{x}\tilde{y}\,d\Omega & -\int_\Omega \tilde{x}\tilde{z}\,d\Omega \\ -\int_\Omega \tilde{x}\tilde{y}\,d\Omega & \int_\Omega \left(\tilde{x}^2 + \tilde{z}^2\right) d\Omega & -\int_\Omega \tilde{y}\tilde{z}\,d\Omega \\ -\int_\Omega \tilde{x}\tilde{z}\,d\Omega & -\int_\Omega \tilde{y}\tilde{z}\,d\Omega & \int_\Omega \left(\tilde{x}^2 + \tilde{y}^2\right) d\Omega \end{bmatrix}.$$

Here $\tilde{x} = x - x_0$, $\tilde{y} = y - y_0$, and $\tilde{z} = z - z_0$ are the coordinates in the frame translated to the element barycenter. From symmetry and positive definiteness properties of I it follows that its unit eigenvectors $\mathbf{e}_1$, $\mathbf{e}_2$, $\mathbf{e}_3$ are mutually orthogonal. Let $\mathbf{e}_1$, $\mathbf{e}_2$, $\mathbf{e}_3$ be a right-hand triple, then the transformation

$$\begin{bmatrix} x_\Omega \\ y_\Omega \\ z_\Omega \end{bmatrix} = \begin{bmatrix} e_{11} & e_{12} & e_{13} \\ e_{21} & e_{22} & e_{23} \\ e_{31} & e_{32} & e_{33} \end{bmatrix} \begin{bmatrix} \tilde{x} \\ \tilde{y} \\ \tilde{z} \end{bmatrix}$$

specifies a rotation of the frame $\tilde{\mathbf{x}} = (\tilde{x}, \tilde{y}, \tilde{z})^{\mathrm{T}}$ to the frame $\mathbf{x}_\Omega = (x_\Omega, y_\Omega, z_\Omega)^{\mathrm{T}}$ of principal axes of the element. In $\mathbf{x}_\Omega$ frame, let us define the preliminary basis functions $\psi_j(\mathbf{x}_\Omega)$ to be monomials of the form

$$\psi_j(\mathbf{x}_\Omega) = s_j^{-1} x_\Omega^{\alpha_j} y_\Omega^{\beta_j} z_\Omega^{\gamma_j}, \quad \alpha_j, \beta_j, \gamma_j \in \mathbb{Z}_+, \quad 0 \le \alpha_j + \beta_j + \gamma_j \le K.$$

The factor

$$s_j = \sqrt{\int_\Omega \left(x_\Omega^{\alpha_j} y_\Omega^{\beta_j} z_\Omega^{\gamma_j} \right)^2 d\Omega}$$

is introduced to guarantee the fulfillment of the normalization condition

$$\int_\Omega \psi_j^2(\mathbf{x}_\Omega) d\Omega = 1 \cdot$$

Next, we orthogonalize the function set $\left\{ \psi_j(\mathbf{x}_\Omega) \right\}$ using the Gram–Schmidt process. This will result in a basis $\left\{ \psi_j^*(\mathbf{x}_\Omega) \right\}$ with the following orthogonality and normalization property:

$$\int_\Omega \psi_i^*(\mathbf{x}_\Omega) \psi_j^*(\mathbf{x}_\Omega) d\Omega = \delta_{ij} \cdot$$

In the initial Cartesian frame, basis functions are then defined as

$$\varphi_j(\mathbf{x}) = \psi_j^*(\mathbf{x}_\Omega(\mathbf{x})), \quad \mathbf{x}_\Omega(\mathbf{x}) = \begin{bmatrix} e_{11} & e_{12} & e_{13} \\ e_{21} & e_{22} & e_{23} \\ e_{31} & e_{32} & e_{33} \end{bmatrix} (\mathbf{x} - \mathbf{x}_0) .$$

All the described transformations preserve the polynomiality of the basis. Orthogonalized and normalized basis built as presented above is resistant to round-off errors, especially in the cases of stretched and strongly curved elements which is crucial for DG method [2]. Returning to the determination of expansion coefficients, let us multiply (1) by a basis function $\varphi_i(\mathbf{x})$ and integrate the resulting expression over the volume of the element:

$$\int_\Omega \left(\frac{\partial \mathrm{U}}{\partial t} + \nabla \cdot \mathbf{F} \right) \varphi_i \, d\Omega = 0, \quad i = 1, \ldots, K_f \cdot$$

Substituting the expansion (2), replacing $(\nabla \cdot \mathbf{F}) \varphi_i$ by $\nabla \cdot (\mathbf{F} \varphi_i) - \mathbf{F} \cdot \nabla \varphi_i$, and applying the Ostrogradsky–Gauss formula, we arrive at the equation system

$$\frac{d \mathrm{u}_i}{dt} + \oint_\Sigma \hat{\mathbf{F}} \cdot \mathbf{n} \varphi_i \, d\Sigma = \int_\Omega \mathbf{F} \cdot \nabla \varphi_i \, d\Omega , \tag{3}$$

where the property

$$\int_\Omega \varphi_i \varphi_j \, d\Omega = \delta_{ij}$$

has been taken into account. Here, Σ is the surface of the element and **n** is its outward unit normal vector. Numerical flux $\hat{\mathbf{F}}$ is introduced due to the possibility of solution discontinuities on element faces. This flux depends on the solution at both sides of a face, U_L and U_R, and also on **n**. To compute the convective numerical flux, Roe formula [3] is adopted:

$$\hat{\mathbf{F}}^{conv}\cdot\mathbf{n}=\frac{1}{2}\left(\mathbf{F}^{conv}(\mathrm{U}_L)+\mathbf{F}^{conv}(\mathrm{U}_R)\right)\cdot\mathbf{n}-\alpha\left|\mathbf{A}_n\right|\frac{\mathrm{U}_R-\mathrm{U}_L}{2}. \qquad (4)$$

In this formula, $\mathbf{A}_n=\partial\left(\mathbf{F}^{conv}\cdot\mathbf{n}\right)/\partial\mathrm{U}$ is Jacoby matrix of convective fluxes normal to the face calculated using the following weighted mean values:

$$\tilde{u}=\frac{\sqrt{\rho_L}u_L+\sqrt{\rho_R}u_R}{\sqrt{\rho_L}+\sqrt{\rho_R}},\quad \tilde{v}=\frac{\sqrt{\rho_L}v_L+\sqrt{\rho_R}v_R}{\sqrt{\rho_L}+\sqrt{\rho_R}},\quad \tilde{w}=\frac{\sqrt{\rho_L}w_L+\sqrt{\rho_R}w_R}{\sqrt{\rho_L}+\sqrt{\rho_R}},\quad \tilde{H}=\frac{\sqrt{\rho_L}H_L+\sqrt{\rho_R}H_R}{\sqrt{\rho_L}+\sqrt{\rho_R}},$$

where $H=E+p/\rho$ is specific total enthalpy.

Let $\{\lambda_i\}$ be the eigenvalues of $\mathbf{A}_n$, and $\mathbf{T}_n$ be the matrix formed by right eigenvectors of $\mathbf{A}_n$. Let us introduce the matrix $\left|\mathbf{L}_n\right|=diag\left(\left|\lambda_i\right|\right)$, then $\left|\mathbf{A}_n\right|$ in (4) can be expressed as $\left|\mathbf{A}_n\right|=\mathbf{T}_n\left|\mathbf{L}_n\right|\mathbf{T}_n^{-1}$.

In (4), α is a coefficient which controls the artificial dissipation. It can take values from 0 (central difference scheme without artificial dissipation) to 1 (a standard upwind Roe scheme). In Taylor–Green vortex test case, it was set to be 0.1 to minimize the artificial viscosity of the scheme. In periodic hill flow test case, a value of 1 was used to maximize the stability of simulations.

Diffusive fluxes at the element face are calculated with the symmetric formula

$$\hat{\mathbf{F}}^{diff}=\frac{1}{2}\left(\mathbf{F}^{diff}(\mathrm{U}_L,\mathbf{G}_L)+\mathbf{F}^{diff}(\mathrm{U}_R,\mathbf{G}_R)\right). \qquad (5)$$

The gradients which enter $\mathbf{F}^{diff}$ in (5) are calculated according to Bassi–Rebay 2 scheme [4].

The surface and volume integrals in (3) are evaluated using the Gaussian quadratures. Cartesian products of one-dimensional Gauss–Legendre (GL) quadrature points are distributed in a standard cube $[-1,1]\times[-1,1]\times[-1,1]$ and in a standard square $[-1,1]\times[-1,1]$, which are then transformed into physical space by serendipity transformations associated with corresponding elements. In Taylor–Green vortex test case, we use $(K+1)$-point one-dimensional GL quadratures due to simplicity of the mesh structure which consists of only cubic cells. In periodic hill flow test case, we adopt overintegration with $(K+2)$-point GL quadratures for better treatment of curvilinear cells.

Consider temporal approximation of (3). Let us transfer the surface integral in (3) to the right hand side of the equation, which then becomes a residual. Denoting the residual vector by $\mathfrak{R}$ and unknown coefficient vector by $\mathfrak{U}$, we arrive at the following form of (3):

$$\frac{d\mathfrak{U}}{dt}=\mathfrak{R}. \qquad (6)$$

Focusing on unsteady simulations, let us use explicit M-step Runge–Kutta approximation of (6):

$$\mathfrak{U}^{(0)} = \mathfrak{U}^{(n)},$$
$$\mathfrak{U}^{(1)} = c_{00}\mathfrak{U}^{(0)} + c_0\,\Delta t\,\mathfrak{R}^{(0)},$$
$$\mathfrak{U}^{(2)} = c_{10}\mathfrak{U}^{(0)} + c_{11}\mathfrak{U}^{(1)} + c_1\,\Delta t\,\mathfrak{R}^{(1)},$$
$$\dots$$
$$\mathfrak{U}^{(k+1)} = c_{k0}\mathfrak{U}^{(0)} + c_{k1}\mathfrak{U}^{(1)} + \dots + c_{kk}\mathfrak{U}^{(k)} + c_k\,\Delta t\,\mathfrak{R}^{(k)},$$
$$\dots$$
$$\mathfrak{U}^{n+1} = \mathfrak{U}^{(M)}.$$

Here, superscripts without brackets indicate time step number while superscripts with brackets indicate internal Runge–Kutta step number.

Within a Δt time step, M Runge–Kutta steps are done, after which the last state of unknown vector $\mathfrak{U}^{(M)}$ is assigned to a new time level $\mathfrak{U}^{n+1}$. The residual $\mathfrak{R}^{(k)}$ is recomputed at each Runge–Kutta step. The coefficients $\{ c_{kl}, c_m \}$ are constant.

The choice of M and $\{ c_{kl}, c_m \}$ determines the temporal order of the scheme. In the present implementation, a 5-step 4th order strong stability preserving Runge–Kutta scheme [5] is employed.

The explicit scheme used is stable only when a number of time step restrictions associated with the approximation of the flux and source terms is satisfied. The time step restrictions have been chosen on the basis of the following conditions:

1) Courant-Friedrichs-Levy restriction related to the approximation of convective fluxes:

$$\tau \le \tau^{conv} = \frac{h}{|\vec{V}| + a},$$

Here h is the smallest distance between the cell barycenter and the centers of each cell faces, a is local sound speed;

2) restrictions associated with the approximation of diffusion fluxes:

$$\tau \le \tau^{diff} = \frac{3\rho h^2}{16(\mu + \mu_T)},$$

eddy viscosity coefficient μ_T to be determined later;

3) restrictions associated with the interaction of convective and diffusive fluxes:

$$\tau \le \tau^{flux} = \frac{4\tau^{diff}}{\left[1 + \sqrt{1 + 4\tau^{diff}/\tau^{conv}}\right]^2};$$

4) restrictions associated with the approximation of the source terms:

$$\tau \le \tau^{source} = \frac{1}{\max_i |\lambda_i^-|},$$

where maximum is taken over all negative eigenvalues of the corresponding Jacobi matrix.

The final time step restriction has the following form:

$$\tau \le C_{stab} \cdot \min\left(\tau^{flux}, \tau^{source}\right),$$

where C_{stab} is the stability coefficient. In the DG method, it depends on the maximum degree of the base polynomials K and it has been determined experimentally.

2.2 “Law of the wall” boundary condition (wall functions)

In the simulations of near-wall turbulent flows using the non-slipping boundary condition, it is necessary for the grid to provide possibility to resolve the main elements in the near-wall zone. It is important to get the correct solution in the viscous sublayer (it determines the viscous friction and heat flux to the wall) and in the buffer zone (where the most of turbulence production takes place).

However, the viscous sublayer thickness is about 0.1% of the total boundary layer thickness. To resolve the processes in the viscous sublayer, it has to contain from 5 to 10 cells. As a result, the size of the near-wall cell should be about 0.01% of the boundary layer thickness. In the case of the DG, this condition must be satisfied at least for the first Gauss point. This reduces the requirements for the first cell size to about 0.1% of the boundary layer thickness: the number of Gauss points in one direction is equal to K+1, and the distribution of Gauss points is non-uniform in vertical direction with a concentration to the wall.

However, even 0.1% of the boundary layer thickness is a very strong requirement for the mesh. Such meshes reduce the efficiency of high-order accuracy methods. If an explicit scheme is used in the simulation, a strong concentration of the grid lines to the wall results in a significant decrease of the convergence rat even when convergence acceleration methods are used such as a local time step. To take full advantage of the high-order accuracy scheme, it is desirable to have the size of the first wall cells up to Y^+=50-100. It can be achieved by the adoption of wall function method. This numerical boundary condition is based on the “wall law", i.e. on a given profile of velocity and other parameters of the boundary layer. It is usually assumed that the flow in a small neighborhood of solid walls can be described using the same self-similar solution as the flow in the boundary layer on the plate. It permits to perform the simulations with much larger near-wall cells than using a non-slipping boundary condition. In the present research, wall law formulation is based on [16].

3. Test Cases

3.1 Taylor–Green Vortex Test Case

The Taylor-Green vortex at the Reynolds number 1600 is a standard test for the code to check its ability to perform the direct numerical simulation of the turbulence [8]. This flow at an initial time moment is defined as a set of large vortices that divided gradually and produce a small-scale quasi-isotropic turbulence (Fig. 2). It is assumed that the simulation will reproduce all the scales of turbulent motion that arise during the evolution of the initial field.

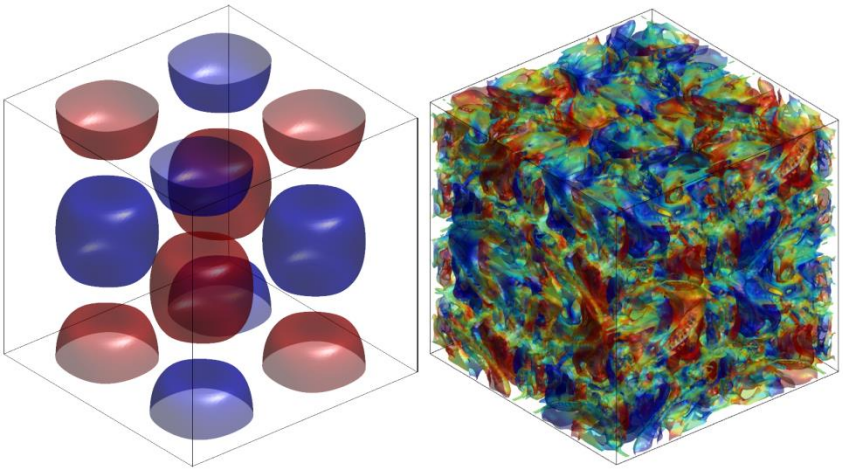

Figure 2. The initial flowfield (pressure isosurface) and the field that is a result of the Taylor-Green vortex evolution

In this paper, the Taylor–Green vortex has been simulated in a cubic computational domain $[-\pi L, \pi L]^3$ with periodic boundary conditions. The grid inside the computational domain has a constant step and it is consisted of identical cells. The simulations have been performed on the grids of 64^3, 96^3, 128^3, 192^3, 256^3, 384^3 and 512^3 cells. The Reynolds number is defined as $\mathrm{Re} = \rho_\infty V_\infty L / \mu$ in this problem, the viscosity coefficient is taken as constant $\mu_\infty = 1.72 \cdot 10^{-5} \frac{kg}{m \cdot s}$ (it is independent of temperature), the initial values of density ρ_∞, velocity V_∞, pressure p_∞, and length scale L are chosen so as to reach $\mathrm{Re} = 1600$ and to obtain the characteristic Mach number $M = V_\infty / \sqrt{\kappa p_\infty / \rho_\infty} = 0.1$. At that, the flow can be considered as incompressible. Below, all variables are dimensioned on a combination of parameters ρ_∞, V_∞ and L.

The initial state of the Taylor–Green vortex is described by the following relations:

$$u = V_0 \sin\frac{x}{L}\ \cos\frac{y}{L}\ \cos\frac{z}{L}, \quad v = -V_0 \cos\frac{x}{L}\ \sin\frac{y}{L}\ \cos\frac{z}{L}, \quad w = 0,$$

$$p = p_0 + \frac{\rho_0 V_0^2}{16}\left(\cos\frac{2x}{L} + \cos\frac{2y}{L}\right)\left(\cos\frac{2z}{L} + 2\right).$$

The main characteristics of this non-stationary flow are the dissipation rate of the turbulence kinetic energy $-d\,\mathrm{E}_k/dt$, which is connected with the turbulent fluctuations that can be resolved by the grid, and enstrophy $\tilde{\varepsilon}$, which is proportional to the energy dissipation at the level of the smallest vortices resolved by the grid. The kinetic energy and entropy are determined by the formulas

$$\mathrm{E}_k = \frac{1}{\langle\rho\rangle\Omega}\int_\Omega \frac{\rho\mathbf{V}^2}{2}d\Omega, \quad \tilde{\varepsilon} = \frac{1}{\langle\rho\rangle\Omega}\int_\Omega \frac{\rho\boldsymbol{\omega}^2}{2}d\Omega$$

where Ω is the computational domain volume, $\langle\rho\rangle$ is average density in the computational domain, $\boldsymbol{\omega} = \mathrm{rot}\,\mathbf{V}$ is vorticity vector. In the simulations, the time dependences of the dissipation rate and enstrophy have been obtained.

The results of the work [9] obtained using the spectral method on a very fine grid are chosen as the reference data. Figure 3 shows a comparison of the results for DG with different degrees of basis polynomials on a grid with 64^3 cells. Figure 3, left presents comparison of the turbulence kinetic energy dissipation rate. It looks acceptable for all tests with $K > 1$. The main contribution to this value is given by large vortices. The time variation of the enstrophy, which is proportional to the energy dissipation at the level of the smallest vortices resolved by the grid, depends on K more strongly than energy (Fig. 3, right).

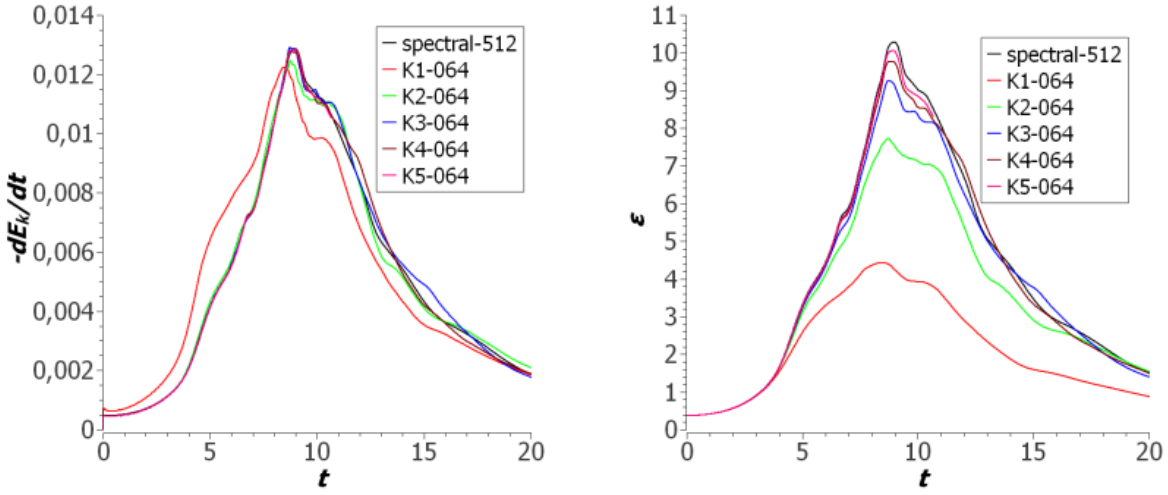

Figure 3. Simulations of the Taylor-Green vortex on a grid of 64^3 cells:
the left picture – the dissipation rate of the turbulence kinetic energy, the right picture - enstrophy

Table 1 summarizes the results obtained using finite volume (FV) and DG methods. The simulations on a grid of 128^3 cells with different reconstructions show that it is impossible to achieve an acceptable accuracy using schemes "Central" and "WENO5". Therefore, further simulations have been performed using "WENO9" only. It should be noted that in the FV method, the number of freedom degrees is equal to the number of grid cells. The second number in each cell indicates the physical simulation time on a cluster that consists of 16 nodes with 32 cores (512 cores in total). The third number (error level) is the difference between the enstrophy maximum obtained in the simulation and the maximum of the reference solution.

If one compares the best solution obtained using the finite volume method ("WENO9", grid of 512^3 cells) and the DG solution obtained in approximately the same physical time ($K = 4$, grid of 96^3 cells), one can see that the DG solution is almost twice as accurate.

Table 1. Results of Taylor–Green vortex simulations

	64^3	96^3	128^3	192^3	256^3	384^3	512^3
FV, «Central»			$2.1\cdot10^6$, 0.36 h., 68%				
FV, «WENO5»			$2.1\cdot10^6$, 0.49 h., 45%				
FV, «WENO9»	$2.6\cdot10^5$, 0.03 h., 63%	$8.8\cdot10^5$, 0.13 h., 50%	$2.1\cdot10^6$, 0.56 h., 38%	$7.1\cdot10^6$, 2.3 h., 23%	$1.7\cdot10^7$, 9.6 h., 16%	$5.7\cdot10^7$, 39 h., 8.0%	$1.3\cdot10^8$, 153 h., 4.7%
DG, $K = 1$	$1.0\cdot10^6$ 0.23 h. 60%	$3.5\cdot10^6$ 1.0 h. 45%	$8.4\cdot10^6$ 3.7 h. 37%				
DG, $K = 2$	$2.6\cdot10^6$ 1.8 h. 25%	$8.9\cdot10^6$ 9.1 h. 13%	$2.1\cdot10^7$ 32 h. 6.9%				
DG, $K = 3$	$5.2\cdot10^6$ 10 h. 10%	$1.8\cdot10^7$ 52 h. 4.2%	$4.2\cdot10^7$ 159 h. 2.2%				
DG, $K = 4$	$9.2\cdot10^6$ 39 h. 5.0%	$3.1\cdot10^7$ 198 h. 1.7%	$7.3\cdot10^7$ 623 h. 0.89%				
DG, $K = 5$	$1.5\cdot10^7$ 136 h. 2.2%						

The table data are presented as a graph in Fig. 4. It can be seen that the DG of the second accuracy order ($K = 1$) is unacceptable for this problem. DG, starting from the third order, demonstrates better efficiency than FV "WENO9". This difference will increase as the required accuracy of the enstrophy calculation increases.

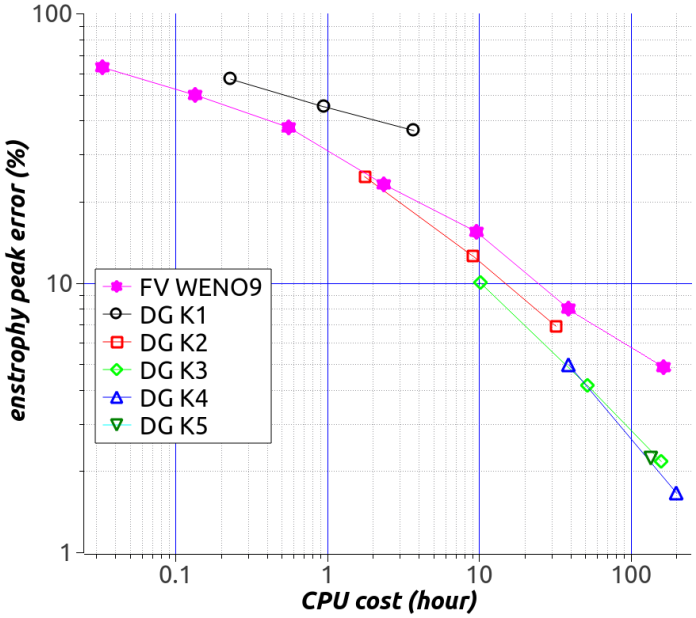

Figure 4. Convergence of the enstrophy peak over the grid and the degree of the DG polynomials

One can conclude that TsAGI code based on the DG $K = 3$ permits to reduce the error in the enstrophy down to 1-2%. It should be noted that using HOM ($K \geq 3$), from the viewpoint of code efficiency, is equivalent to implementation of low order scheme on larger grids but requires less computational time, making HOM an attractive option, especially when the problem is solved with high accuracy goal.

3.2 Parallel version of computational code and scalability

The Taylor-Green vortex test case was also employed to assess the scalability of the presented method on an HPC cluster.

The upper level of the parallel program model is based on geometric parallelism. The computational domain consists of a set of cells (finite elements) and relationships between them. For a numerical scheme, grid data are defined by a set of three types: cell data, cell side data and node data. The topology of cell connections is described by a dual grid graph, where the vertices are the cell borders, and the edges are the faces between the vertices. The grid data structure is supplemented with a set of boundary sides. The computational domain is divided between parallel processes into subdomains by rational decomposition of the grid graph. The decomposition is performed with the use of the ParMETIS library. For each grid cell, the number of the owner process is determined. So, the cells are distributed among the subdomains. For each subdomain, when starting the simulation, new cells are added, so-called fictitious cells, intended to store the data from neighboring subdomains. The calculation in these cells is not performed.

The middle level of the parallel program model involves shared memory exchange within a multi-thread parallel system. OpenMP library is commonly used for this purpose, although MPI can also be employed for simplicity of implementation.

One of the main advantages of the Galerkin method with discontinuous basis functions is the compactness of the numerical scheme stencil. The calculation of viscous flows is performed using the BR2 method [4] which also uses a compact template. Therefore, the code creates only one layer of the fictitious cells. After each internal stage of the Runge–Kutta procedure, data are exchanged between the processes. Such a simple organization of the parallel computing algorithm, together with the high computational costs of the method per cell, which increases with the growth of K, permits to achieve a highly efficient implementation.

The scalability test, i.e. the acceleration measurement depending on the amount of computing resources used, has been performed on a supercomputer [10]. All computing nodes were identical, each of them had 12 CPU cores. The simulation grid for the Taylor–Green vortex contained 128^3 (2 097 152) cells.

The resulting graphs of acceleration are shown in Figure 5 on a logarithmic scale. For clarity, the lines are drawn corresponding to the parallel efficiency of 100% (max, red dotted line), when each doubling of the core number results in acceleration of 2 times, and of 90% (desired, black dashed line), when each doubling of the core number results in acceleration of 1.9 times. The results are shown for $K = 3$ and for $K = 4$.

The green curves correspond to the parallel model, where MPI is used at both the upper and middle levels. There is a tendency to a significant decrease in efficiency when the number of cores exceeds 2 thousand. This shows that the overhead associated with the implementation of exchanges and the imbalance in the process load begins to prevail over the gain due to increase of computing resources. Transition to a parallel model, where OpenMP is used at the middle level, helps to reduce this overhead. It can be seen that the blue curves corresponding to this model demonstrate a high level of parallel efficiency (at least 90%) up to 6 thousand cores in the case of scheme $K = 3$ (350 grid cells per core) and up to 12 thousand cores in the case of scheme $K = 4$ (175 grid cells per core). To achieve high efficiency with more CPU cores, an additional research is necessary. Apparently, the main reason of the efficiency decrease with a larger number of cores is the increase of overhead costs due to insufficient power that has been used in the computational grid tests: the number of grid cells per CPU core becomes less than 150, and the time of useful calculations becomes comparable to the time spent on data exchange between processes. If this assumption is correct, then the efficiency of simulations on several dozens of thousands of cores will increase in the case of solving the problems with a significantly larger number of grid cells.

A comparison of the graphs in Figure 5 on the left ($K = 3$) and on the right ($K = 4$) shows that with an increase in K, the code scalability improves, and, in this case, it permits to use efficiently (with an acceleration of about 1.8) twice as many CPU cores. It is a natural consequence of the fact that as K increases, the computational cost per cell increases, and the overhead increases more slowly due to the compactness of the scheme mentioned above.

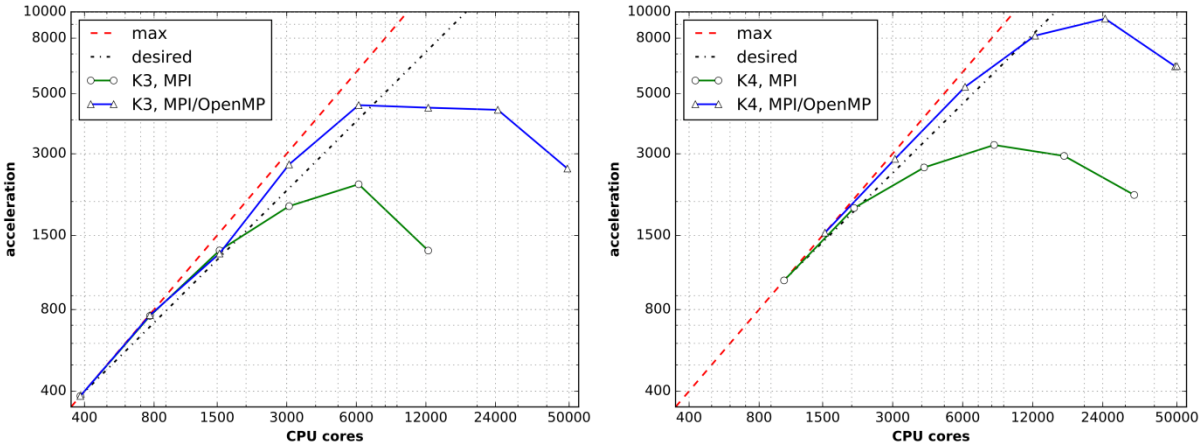

Figure 5. Scalability of the solver code in the Taylor-Green vortex problem. The simulation grid contains 128^3 cells. The left figure corresponds to scheme *K*=3, the right figure to *K*=4

3.3 Simulation of a circular subsonic jet in stagnant surroundings

The high Reynolds number of this test case, $Re_D \approx 5\times10^5$, does not allow to conduct a DNS. Instead, the ability of TsAGI code to perform an underresolved simulation was studied in this test case. The explicit subgrid stresses were switched off since their influence in turbulent jets is usually not decisive. This corresponds to ILES method.

The outflow of a circular subsonic jet from a single-contour nozzle into a stagnant air has been considered. The jet, which was investigated experimentally in NASA Glenn Research Center [14], was simulated to obtain the "reference" data on jets at high Reynolds numbers that are characteristic for passenger aircraft engines (Mach numbers from 0.5 to 1.0, the ratio of static temperatures T_{jet}/T_∞ from 0.83 to 2.70, the nozzle pressure ratio π_c from 1.1 to 1.9). Among the available regimes, the cold subsonic flow regime SP3 has been selected: Mach number at the cross section 0.513, T_{jet}/T_∞ = 0.950, π_c = 1.197.

The nozzle geometry, the computational grid for RANS-based modeling and experimental data are available on the NASA website [15]. The data contains the axial distributions of the dimensionless average velocity U/U_{jet} and the kinetic energy of turbulence

$$\frac{k}{U_{\text{jet}}^2} = \frac{\overline{u'^2} + \overline{v'^2} + \overline{w'^2}}{2U_{\text{jet}}^2},$$

as well as the transversal profiles of the velocity components U/U_{jet}, V/U_{jet}, shear stresses $\overline{u'v'}/U_{\text{jet}}^2$ and kinetic energy of turbulence k/U_{jet}^2.

For ILES, a cylindrical computational domain that covers a full circle in the azimuthal direction has been taken. The length of the computational domain from the nozzle exit to the outlet is 40*D*, where *D* = 5.08 cm is the nozzle exit diameter. The radius of the computational domain varies from 25*D* to 30*D*. In the computational domain, a structured hexahedral second order (piecewise-parabolic) grid is generated, as shown in Fig. 6. It contains 100 thousand cells. To save the computational resources, it has been decided to exclude the simulation of the boundary layer. It relaxed the requirements for concentrating the mesh lines near the nozzle surfaces. The grid allows to resolve the structure of large vortices at the distance of 20*D* from the nozzle. It corresponds to the range of available experimental data.

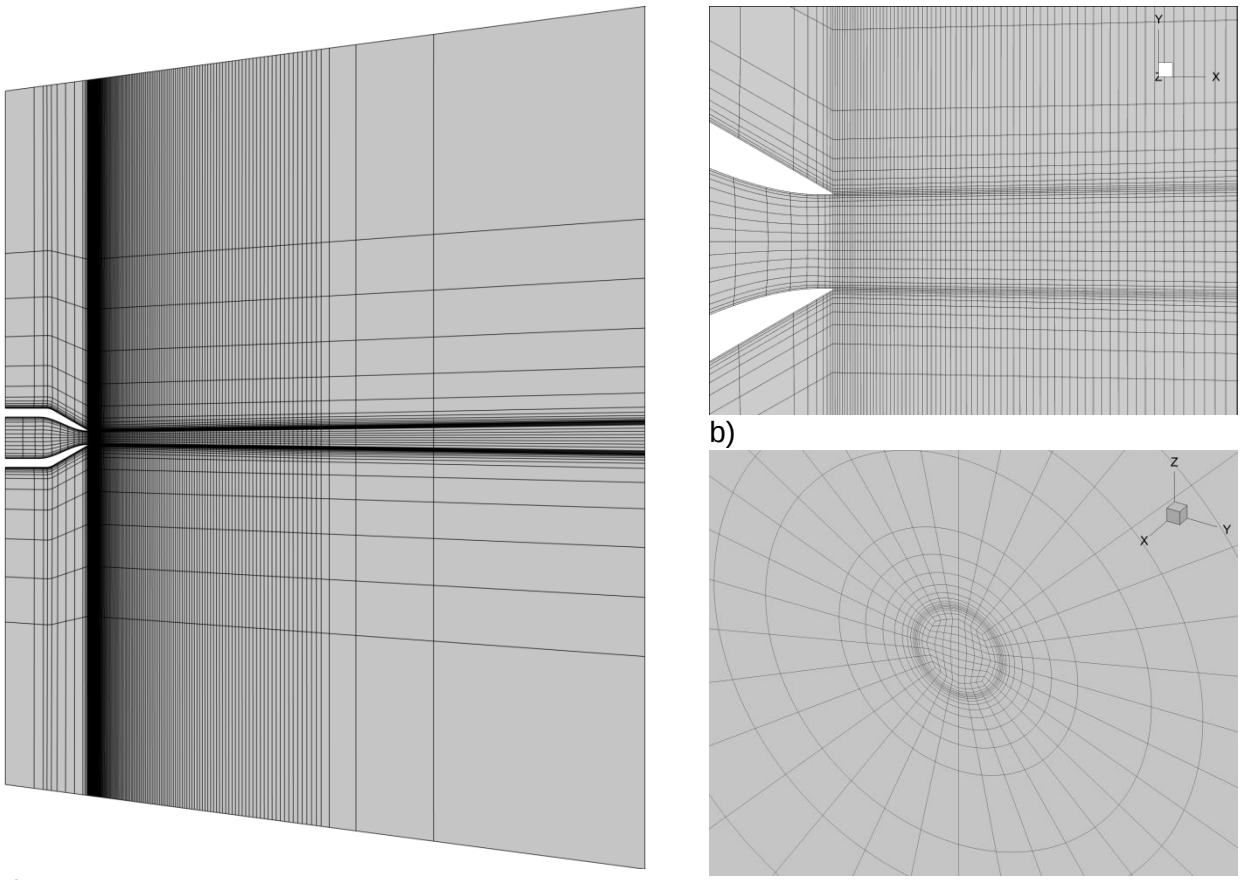

a) b) c)

Figure 6. Simulation grid for DG (round jet): a) the cross-section of the grid with the *x*-*y* plane, b) a part of this cross-section near the nozzle edge,
c) the cross-section with the *y*-*z* plane near the nozzle edge

The inflow boundary condition with a weak superimposed flow $M = 0.01$ is chosen at the inlet boundaries outside the jet, and the constant pressure boundary condition is chosen at the outlet. p_0 and T_0 are specified at the inlet inside the nozzle, and slip wall boundary condition is chosen on the nozzle walls.

The simulations have been performed with $K = 2$ and $K = 3$. The simulations have started from a uniform mean field. Turbulence has not been generated artificially at the inlet boundary: it emerged in the mixing layers of jet due to the evolution of round-off errors on the basis of Kelvin-Helmholtz instability. The instantaneous fields of the Mach number M in the steady-state flow regime are shown in Fig. 7 and 8. In the simulation with $K = 3$, smaller vortex structures are resolved than in the simulation with $K = 2$.

After the flow regime has been established (5 flow passes along the distance of 20D), the accumulation of statistical data (the average fields of gas parameters and correlations $\overline{u_i' u_j'}$) has begun, which lasted during the time corresponding to 200 flow passes through the computational domain. The fields of $\overline{M}$ and $\overline{u'^2}/U_{\text{jet}}$ obtained in the simulation with $K = 3$ are shown in Fig. 9 and 16. A peak in the pulsation level is visible at the beginning of the mixing layer. It corresponds to the evolution of the jet from a flow that does not contain pulsations in the near-wall zone of the nozzle. In this case, the growth rate of the jet mixing layer width is locally overestimated.

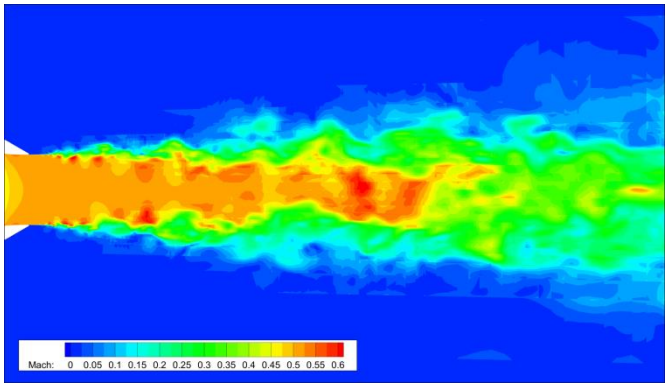

Figure 7. Instantaneous field of the Mach number in a circular jet. Simulation with *K* = 2

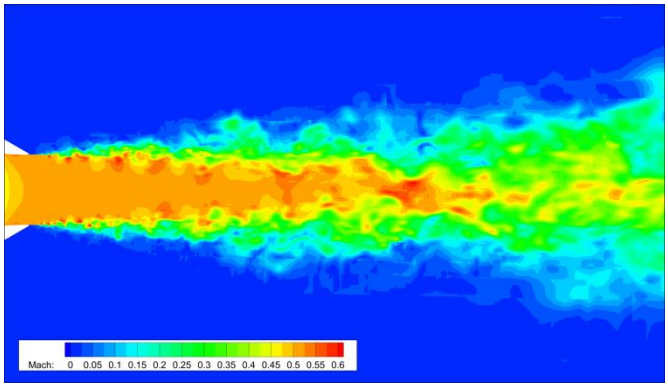

Figure 8. Instantaneous field of the Mach number in a circular jet. Simulation with *K* = 3

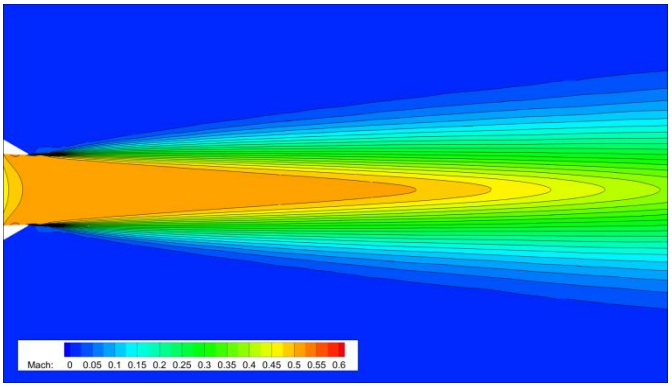

Figure 9. The field of the average Mach number. Simulation with *K* = 3

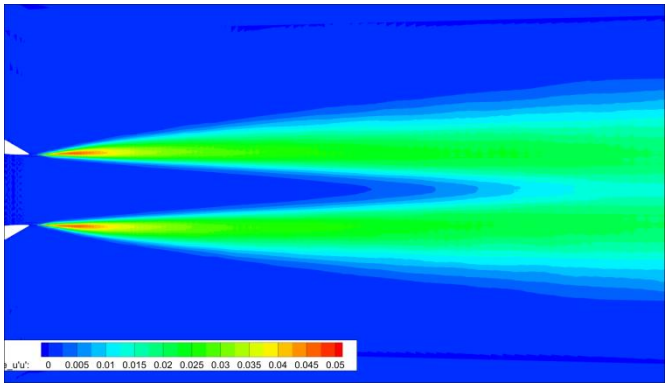

Figure 10. Field $\overline{u'^2}/U_{\text{jet}}^2$. Simulation with *K* = 3

Figure 11 shows a comparison of the axial velocity distributions U/U_{jet} obtained in the simulations for *K* = 2 and *K*=3 with the experiment and simulations of other authors, and Figure 12 shows a

similar comparison of the axial distributions of the turbulence kinetic energy k/U_{jet}^2 (Fig. 10) and the level of streamwise velocity pulsations $\sqrt{\overline{u'^2}}/U_{\text{jet}}$. It is obvious that the resolution of the chosen grid is not sufficient for the simulation with $K = 2$. The length of the initial region, which is equal to the distance between the nozzle exit and the section where the axial velocity decreases by 1% of the velocity in the jet core, is underestimated by 29%. The maximum kinetic energy level is also overestimated by an amount of about 35%. With the transition to $K = 3$, both profiles significantly approach the experimental data.

In Figures 11 and 12, in addition to the experimental data [14] and numerical data [16, 17, 18] on an almost identical jet (Mach number at the exit is 0.58, temperature ratio $T_{\text{jet}}/T_{\infty}$ = 0.97, nozzle exit diameter D = 5.08 cm) are plotted. The axial distributions of the mean velocity in the two experiments are almost identical. In all LES data, the length of the initial part is underestimated by 10-30%. DG simulations with $K = 3$ are closest to the experimental data (underestimation of the initial part length by 12%). The same conclusion can be made when the distributions $\sqrt{\overline{u'^2}}/U_{\text{jet}}$ along the jet axis are compared. The SST turbulence model for RANS gives the result that is the farthest from the experimental data. It significantly overestimates the length of the initial part of the jet (by 51%) and does not describe a smooth growth of pulsations on the jet axis at the boundary between its initial and transition parts. The maximum value of the turbulence kinetic energy on the jet axis in the ILES simulation with $K = 3$ is overestimated by 3.5%, and in the RANS/SST simulation by 22.5%.

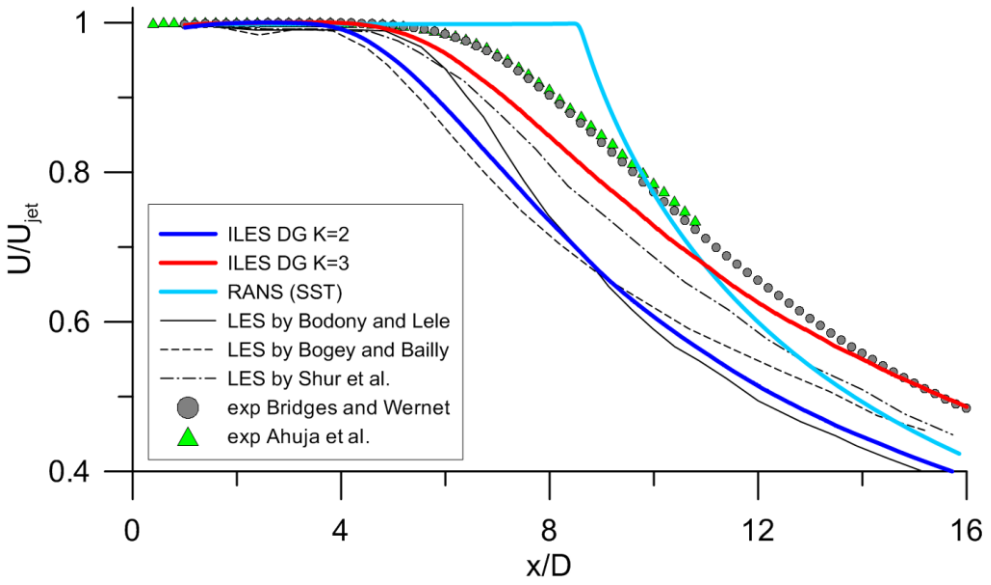

Figure 11. Axial distributions of velocity in a circular jet. Simulations with $K = 2$ and $K = 3$ and their comparison with the experiment and with simulations of other authors using the RANS and LES methods

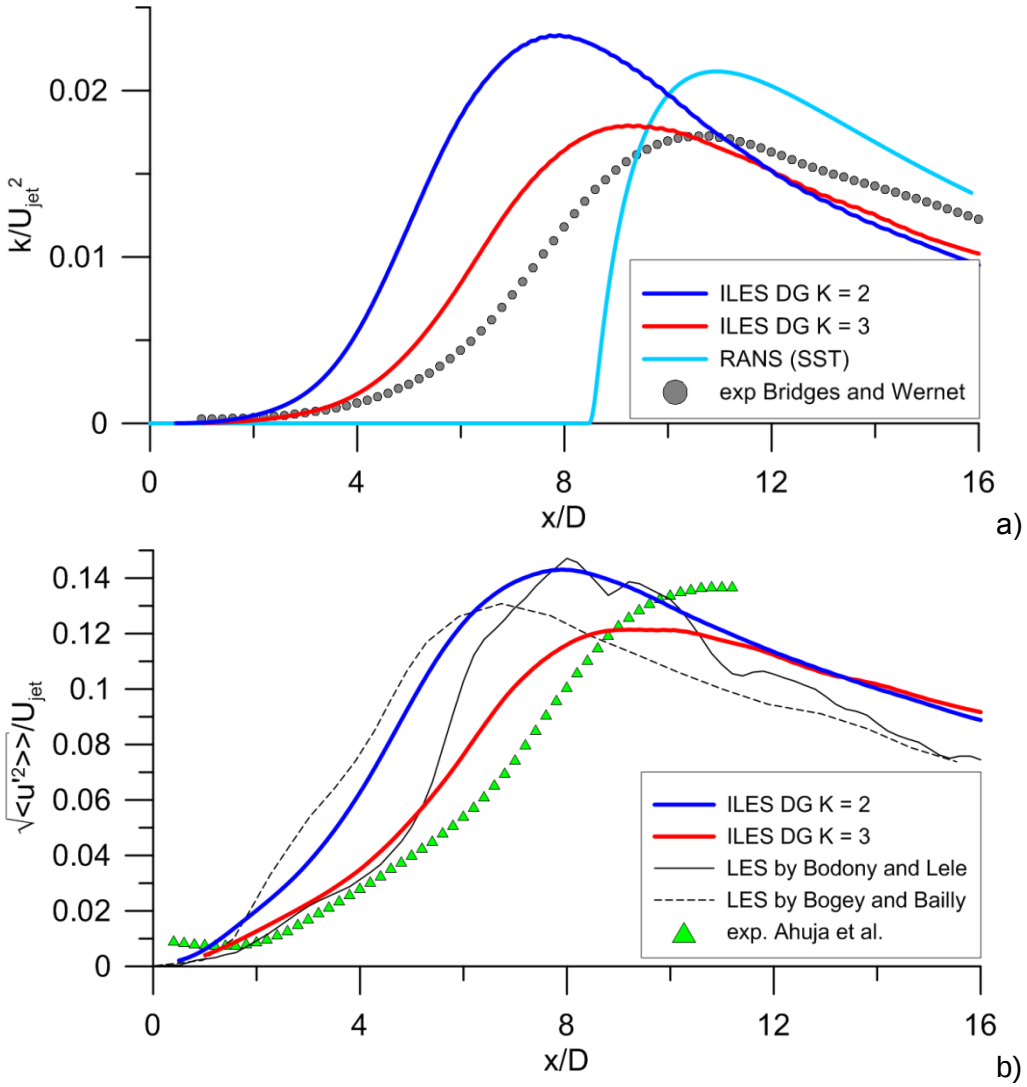

Figure 12. Axial distributions of velocity pulsations in a circular jet. Simulations with $K = 2$ and $K = 3$ and their comparison with the experiment and simulations of other authors using the RANS and LES methods. a) distribution of the turbulence kinetic energy;
b) distributions of the root-mean-square pulsations of the streamwise velocity

Finally, in Fig. 13 and 14, the transverse profiles of velocity, turbulence kinetic energy and shear stresses $\overline{u'v'}/U_{\text{jet}}^2$ are compared with the experiment. The characteristic sections $x / D = 5$ (the end of the initial section of the jet) and $x / D = 10$ (the transition section) are taken.

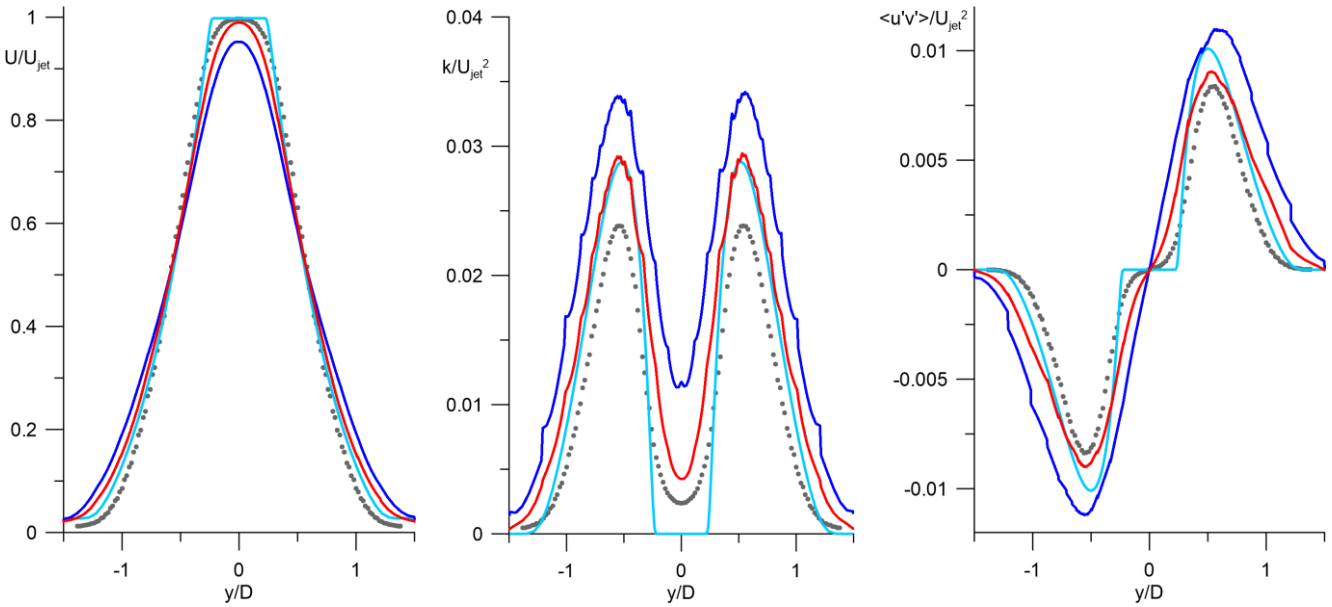

Figure 13. Transverse profiles of the average velocity (a), the turbulence kinetic energy (b) and $\overline{u'v'}/U_{\text{jet}}^2$ (c) in the section $x / D = 5$. Designations as in Fig. 11

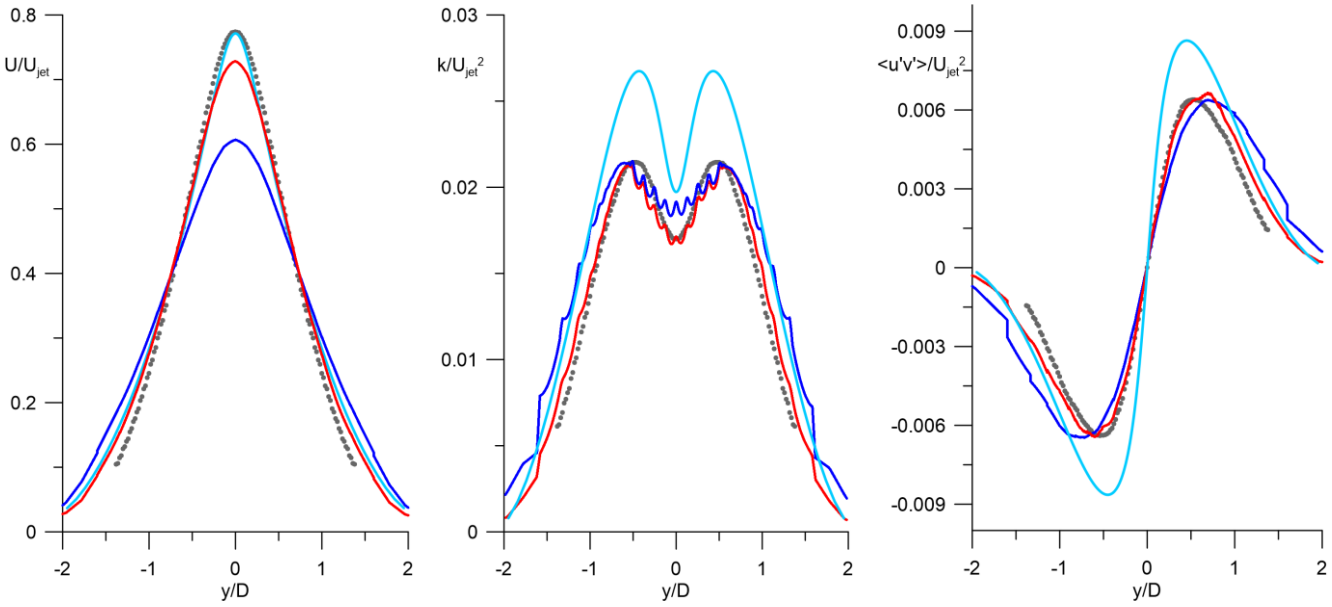

Figure 14. Transverse profiles of the average velocity (a), the turbulence kinetic energy (b) and $\overline{u'v'}/U_{\text{jet}}^2$ (c) in the section $x / D = 10$. Designations as in Fig. 11

In the section $x / D = 5$, the influence of the overestimated turbulence level in the simulation is visible: the width of the mixing layers and the profiles of the turbulence parameters are distorted. The transition from $K = 2$ to $K = 3$ reduces the level of discrepancies by at least half.

In the section $x / D = 10$, the turbulence reaches the equilibrium level corresponding to the experimental data. On the other hand, the jet width, especially in the simulation with $K = 2$, is overestimated due to the incorrect velocity of the mixing layer development upstream.

As for the results of RANS simulations, one can note that the turbulence kinetic energy and shear stress levels are described correctly in the initial part and it are overestimated by 20-30% in the transition section. The jet width of the in both zones is simulated satisfactorily.

The data obtained confirm the applicability of DG-based ILES in high Reynolds number jet flow. Higher accuracy in comparison with RANS was demonstrated in describing the initial and transition jet regions. The presented results were at least of the same quality as FV LES simulations of other authors. For the considered grid power, it is recommended to conduct the jet simulations with *K* equal to at least 3 to satisfactory resolve the vortex flow structure.

3.4 Periodic Hill Flow Test Case

The final test case is Periodic hill flow [11]. Compared to the previous flows, this test case deals with the solid walls, which is the most common situation for aerodynamic flows. Important feature of this test is pressure-induced separation which is rarely modeled in RANS computations correctly. From another viewpoint, this test is very convenient to validate LES/DES solvers. Well-described boundary conditions, including periodic law in streamwise direction, make this test case easily formulated in a scale-resolving simulation.

Three kinds of simulations were performed, namely ILES, DDES without wall functions and DDES with wall functions. The aim of the test case was to assess the accuracy of different techniques in describing the near-wall features of the flow.

A flow over a set of identical smooth-shaped hills was studied. The geometry of the hills was formulated by means of cubic polynomials [9]. Let us take specific length h to be hill height, then the channel height above the hill crest is $2.035h$, distance between the hills is $9h$, and spanwise length is $4.5h$. Characteristic (bulk) velocity U_b is the mean velocity of the flow over the hill crest, characteristic time is $t_c = 9h/U_b$. Bulk Mach number $M_b = U_c/\sqrt{\gamma RT_w}$ is set to be 0.1, where T_w is wall temperature. Reynolds number $\mathrm{Re} = \bar{\rho}U_b h/\mu$ is 10595, where $\bar{\rho}$ is mean density of the fluid over the flow domain. To support the specified mass flow rate, a dynamically adjusted streamwise pressure gradient $(dp/dx)_{imp}$ was added to the momentum equation according to the formula

$$\left(\frac{dp}{dx}\right)_{imp}^{n+1} = \left(\frac{dp}{dx}\right)_{imp}^{n} - \frac{1}{\Omega\,\Delta t}\left(MFR_V^* - 2\,MFR_V^n + MFR_V^{n-1}\right),$$

where Ω is computational domain volume, Δt is time step, *n* is current step number, MFR_V^* is required mass flow rate averaged over the whole computational domain, while MFR_V^k is actual mass flow rate at time step k. From our viewpoint, this method is more robust than averaging only over hill crest, which can produce oscillations of mass flow rate.

8 ILES simulations were performed: *K* = 1, 2, 3, 4, 5 on 32x16x16 mesh and *K* = 1, 2, 3 on 64x32x32 mesh. 4 DDES simulations without wall functions were *K* = 2, 3 on 32x16x16 mesh and *K* = 2, 3 on 64x32x32 mesh, and the same simulations were repeated with wall functions. All meshes were obtained by coarsening a baseline $512\times256\times256$ mesh from Ref. 12. The element edges were taken to be piecewise-parabolic, see Fig. 15.

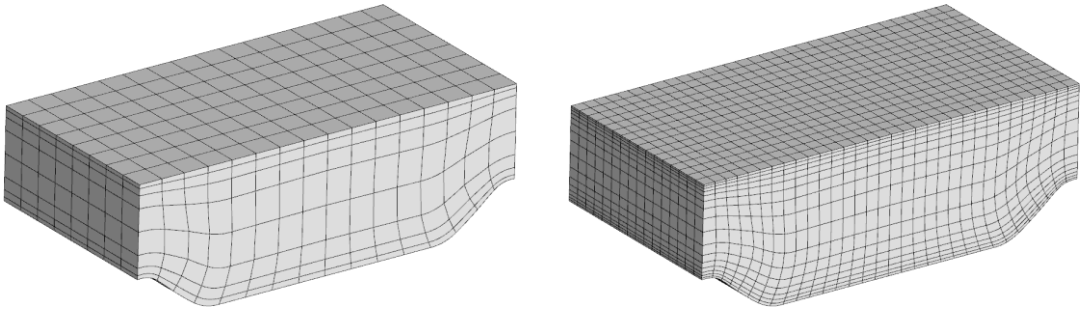

Figure 15. Computational meshes: 16×8×8 (left) and 32×16×16 (right)

All simulations were started from uniform initial flow field. Statistically steady flow appeared within a time period of $30t_c$. After $t = 30t_c$, mean fields of velocity components and correlations between their fluctuations were averaged during a period of $100t_c$. After temporal step, additional averaging over span (z axis direction) was performed.

A series of velocity and turbulence profiles in three cross-sections was extracted from the computational flow fields. The cross-sections are shown in Fig. 16. The first one at $x/h = 0.05$ corresponds to hill crest, the second at $x/h = 3$ is taken near the end of separation zone, while the third at $x/h = 6$ is placed in the recovery region. The results of LES computations from Ref. 13 were used as the reference data.

In Fig. 17, velocity profiles obtained with ILES on 32x16x16 mesh are compared to the reference data. Almost converged solution is observed with K ≥ 3. Recirculation zone length is slightly underestimated which may be due to deficiency of ILES approach near the walls. In Fig. 18, transverse Reynolds stress profiles $\overline{v'^2}$ are depicted. Polynomial convergence is seen to be slower for the second moments than for the mean field. From Fig. 17 and 18 it is also seen that *K* = 1 solution is incompatible with the chosen mesh density.

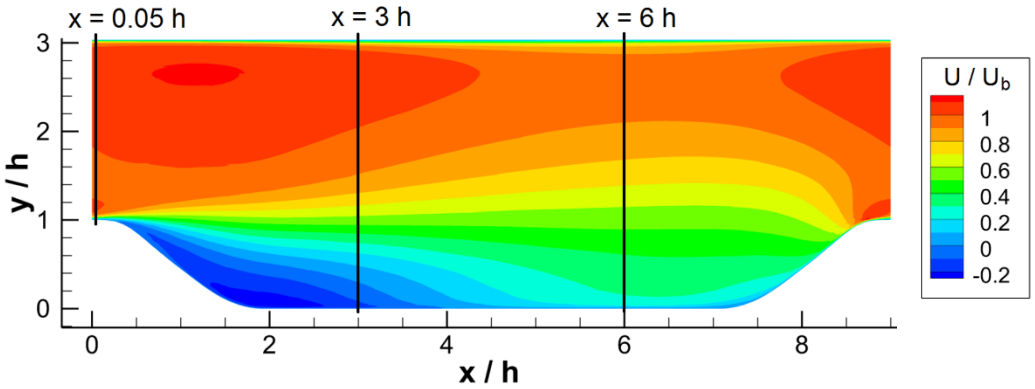

Figure 16. Cross-sections selected for comparison with reference data

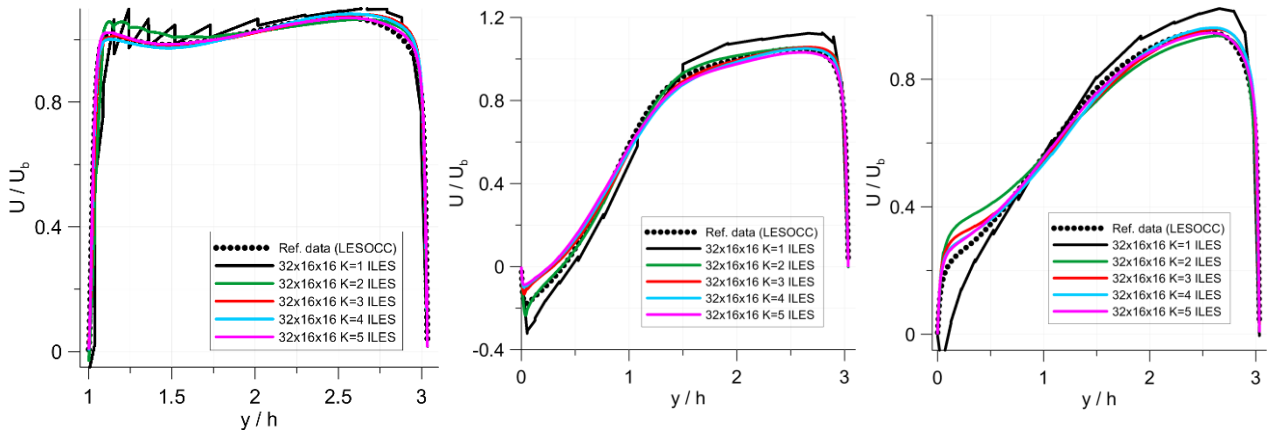

Figure 17. Mean streamwise velocity profiles, ILES simulations on 32x16x16 mesh. Cross-sections: *x* / *h* = 0.05 (left), *x* / *h* = 3 (middle), *x* / *h* = 6 (right)

In Fig. 19 and 20, mean velocity and transverse Reynolds stress fields obtained in ILES on 64x32x32 mesh are compared. It is seen that K = 3 solution on a finer mesh closely corresponds to K = 5 solution on a coarser mesh. On both meshes, K = 1 solutions are too underresolved.

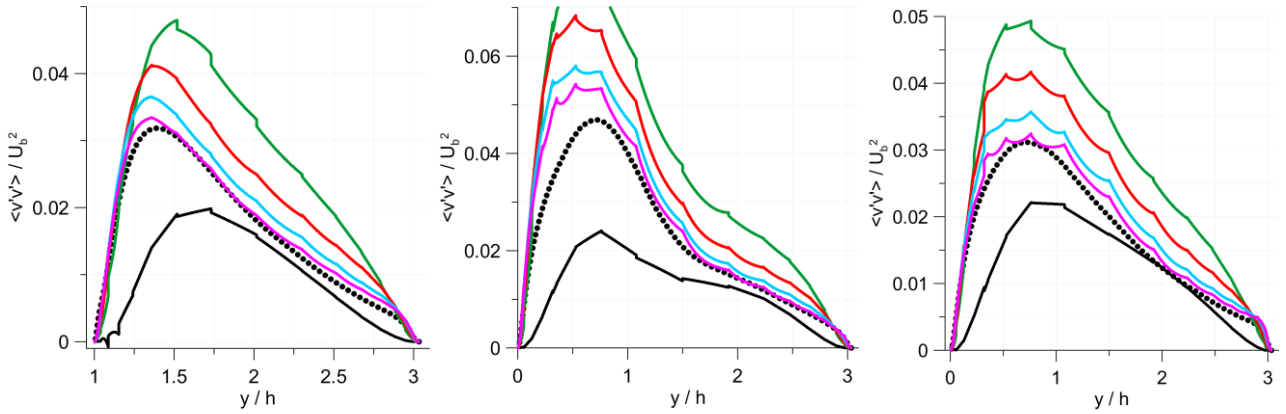

Figure 18. Transverse Reynolds stress profiles $\overline{v'^2}$, ILES simulations on 32x16x16 mesh. Cross-sections: *x* / *h* = 0.05 (left), *x* / *h* = 3 (middle), *x* / *h* = 6 (right). Designations as in Fig. 8

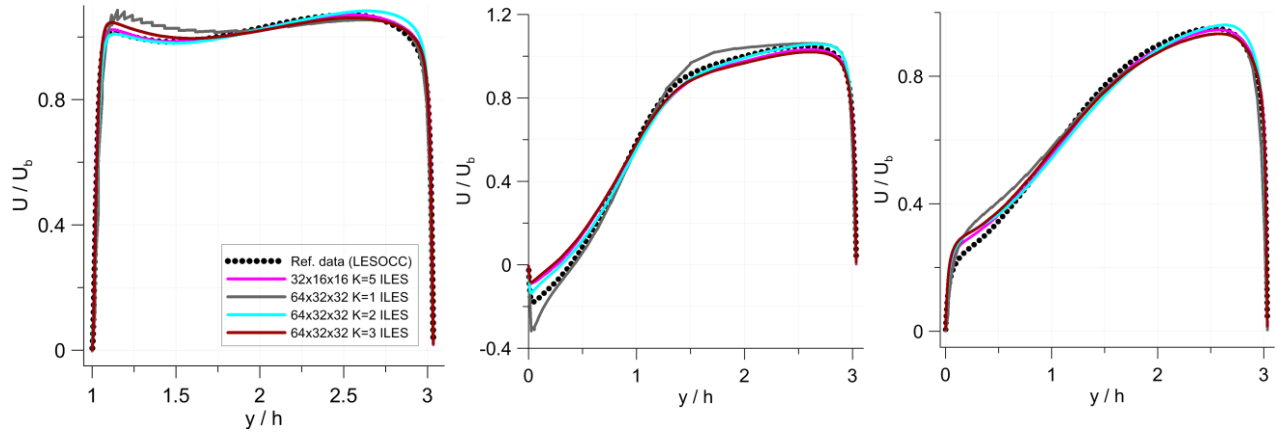

Figure 19. Mean streamwise velocity profiles, ILES simulations on 64x32x32 mesh. Cross-sections: *x* / *h* = 0.05 (left), *x* / *h* = 3 (middle), *x* / *h* = 6 (right)

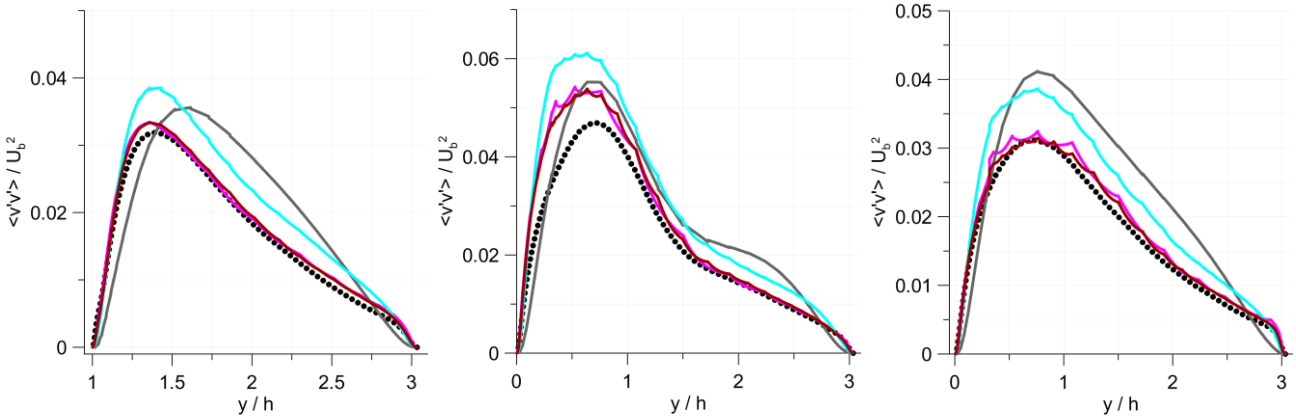

Figure 20. Transverse Reynolds stress profiles $\overline{v'^2}$, ILES simulations on 64x32x32 mesh. Cross-sections: *x* / *h* = 0.05 (left), *x* / *h* = 3 (middle), *x* / *h* = 6 (right). Designations as in Fig. 10

Finally, in Fig. 21 and 22, DDES solutions are compared with ILES and the reference data. Introduction of explicit subgrid model clearly improves the solution in terms of mean profiles in separation zone. On the other hand, switch from no-slipping boundary condition to wall functions results in deterioration of the solution, particularly in reducing the of separated zone length. Attached flow regions are relatively insensitive to wall treatment. This result indicates the limitations of wall functions near the separation and reattachment points.

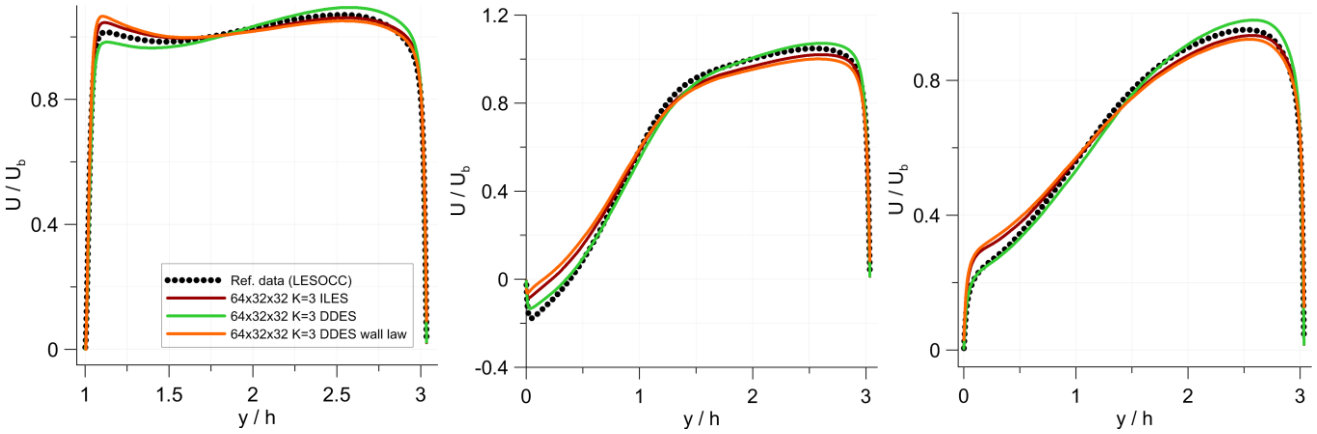

Figure 21. Mean streamwise velocity profiles, ILES vs. DDES, 64x32x32 mesh, K = 3.
Cross-sections: x / h = 0.05 (left), x / h = 3 (middle), x / h = 6 (right)

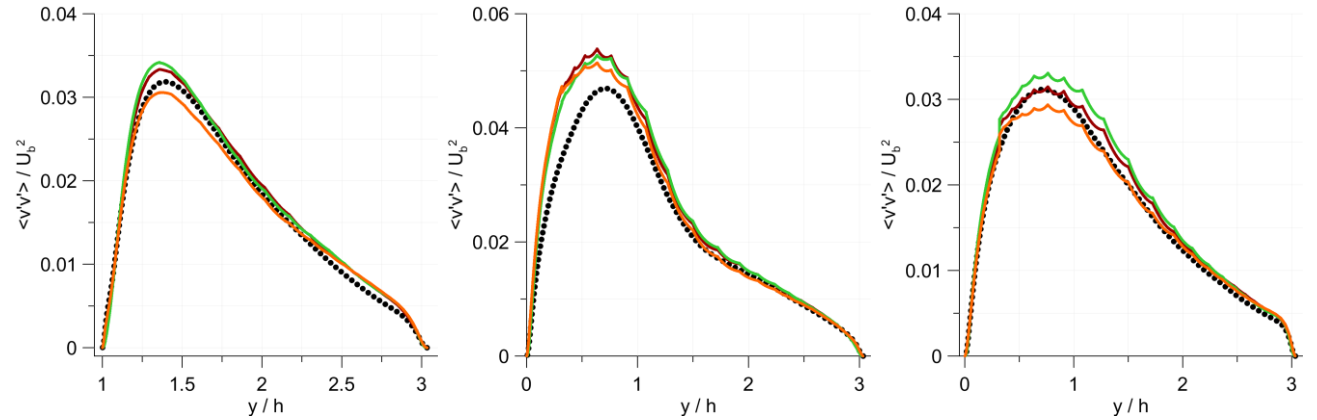

Figure 22. Transverse Reynolds stress profiles $\overline{v'^2}$, ILES vs. DDES, 64x32x32 mesh, K = 3.
Cross-sections: x / h = 0.05 (left), x / h = 3 (middle), x / h = 6 (right). Designations as in Fig. 10

To sum up, performed Periodic Hill Flow simulations look promising because they allowed to obtain results similar to reference data with DG K=3 on as coarse mesh as 32x16x16 cells. This setting corresponds to 1.63×10^5 degrees of freedom while the reference 2nd order simulation was performed with 13.1×10^6 degrees of freedom.

4. Conclusion

Unsteady Discontinuous Galerkin method presented in the paper was studied in parallel scale-resolving simulations of three turbulent flows.

In Taylor–Green vortex test case, advantage over finite volume schemes (WENO and centered) was demonstrated in CPU cost needed to obtain the required enstrophy prediction accuracy. This advantage becomes greater as the accuracy requirements grow. The most efficient schemes in this test case were DG with polynomial orders $K \geq 3$. Scalability was assessed on a 50,000 core HPC cluster. It was shown that speed-up was nearly linear, about 1.9 times with each CPU core number doubling, up to 12,000 cores, and was probably limited by the size of the test problem.

In subsonic jet test case, the simulations based on the developed methodology in the ILES framework provided higher accuracy, compared to RANS, in describing the initial and transition jet regions. The simulation with K = 3 predicted the potential core length with an underestimation of about 10% compared to 50% overestimation of the corresponding RANS simulation based on the SST turbulence model. The maximum kinetic energy of turbulence on the jet axis in the simulation with K = 3 was predicted with 3.5% error as opposed to 22.5% error in RANS/SST simulation. The presented results demonstrated at least the same quality as FV LES simulations of other authors.

In periodic hill flow, DG simulations on $32 \times 16 \times 16$ mesh with DG $K = 3$ compared favorably against reference data despite 10 times lower number of degrees of freedom. Explicit subgrid model

improved the prediction of the separation zone. On the other hand, wall functions spoiled the solution in recirculation region, indicating the limitation of this approach under separated flow conditions.

Obtained results allow to consider the developed DG method as promising for practical applications.

References

[1] Arnold, D. N., and Awanou, G., "The Serendipity Family of Finite Elements," Foundations of Computational Mathematics, Vol. 11, No. 3, 2011, pp. 337-344.

[2] Bassi, F., Botti, L., Colombo, A., Di Pietro, D. A., and Tesini, P., "On the flexibility of Agglomeration Based Physical Space Discontinuous Galerkin Discretizations," Journal of Computational Physics, Vol. 231, No. 1, 2012, pp. 45-65.

[3] Roe, P. L., "Approximate Riemann Solvers, Parameter Vectors, and Difference Schemes," Journal of Computational Physics, Vol. 43, No. 2, 1981, pp. 357-372.

[4] Bassi, F., Rebay, S., Mariotti, G., Pedinotti, S., and Savini, M., "A High-Order Accurate Discontinuous Finite Element Method for Inviscid and Viscous Turbomachinery Flows," *2nd European Conference on Turbomachinery – Fluid Dynamics and Thermodynamics, Technologisch Instituut*, March 5-9, 1997.

[5] Gottlieb, S., Shu, C.-W., and Tadmor, E., "Strong Stability-Preserving High-Order Time Discretization Methods," *SIAM Review*, Vol. 43, No. 1, 2001, pp. 89-112.

[6] Visbal M. R., Morgan P. E., Rizzetta D. P. An implicit LES approach based on high-order compact differencing and filtering schemes //AIAA paper. – 2003. – T. 4098. – C. 2003.

[7] Spalart P.R., Deck S., Shur M.L., Squires K.D., Strelets M.Kh., Travin A. 2006. A new version of detached-eddy simulation, resistant to ambiguous grid densities. Theor. Comp. Fluid Dyn. 20:181–95.

[8] Taylor G.I., Green A.E. Mechanism of the production of small eddies from larger ones // Proc. Royal Soc. A. – 1937. – Vol. 158, no. 895. – P. 499-521. — URL: http://www.jstor.org/stable/96892.

[9] W.M. Van Rees, A. Leonard, D.I. Pullin, and P. Koumoutsakos. "A comparison of vortex and pseudo-spectral methods for the simulation of periodic vortical flows at high Reynolds number". // Journal of Computational Physics. — 2011. — Vol.230. — PP. 2794–2805.

[10] Collective Use Center URL: http://www.vniief.ru/wps/wcm/connect/vniief/site/partnership/ckp/computing

[11] Mellen, C. P., Frohlich, J. and Rodi, W., "Large Eddy Simulation of the Flow Over Periodic Hills," *16th IMACS World Congress*, 21–25 August, 2000.

[12] 4th International Workshop on High-Order CFD Methods, http://how4.cenaero.be.

[13] Breuer, M., Peller, N., Rapp, C., and Manhart, M., "Flow over Periodic Hills – Numerical and Experimental Study over a Wide Range of Reynolds Numbers," *Computers and Fluids*, Vol. 38, 2009, pp. 433-457.

[14] J. Bridges, M. P. Wernet. Establishing consensus turbulence statistics for hot subsonic jets," AIAA Paper 2010-3751, 2010.

[15] Axisymmetric Subsonic Jet. NASA Langley Research Center, Turbulence Modeling Resource.– URL: https://turbmodels.larc.nasa.gov/jetsubsonic_val.html

[16] Nichols, R.H. and Nelson, C.C., 2004. Wall function boundary conditions including heat transfer and compressibility. AIAA journal, 42(6), pp.1107-1114.

1. Copyright Issues

The copyright statement is included in the template and must appear in your final pdf document in the position, style and font size shown below. If you do not include this in your paper, ICAS is not allowed and will not publish it.

2. Archiving

The ICAS 2021 proceedings will receive an ISBN number and will be cataloged and archived by the German National Library.

3. Sending Your Electronic Paper & Contacting the Editor of the Electronic Proceedings

Please refer to section 2.2 and follow the submission method described there.

For question concerning the paperlayout please contact:
icas-publications@dglr.de

For questions concerning the online paper handling system please contact:
icas-techadmin@dglr.de

Only if you do not have web access the electronic files may also be sent by mail on CD/CDRW, to the address
Deutsche Gesellschaft für Luft- und Raumfahrt - Lilienthal-Oberth e.V.
Godesberger Allee 70
53175 BONN
GERMANY

4. Submission Dates

Since the Proceedings will be published on a CD ROM, distributed at the Congress and will be downloadable at the ICAS archive, it is essential that:

- The written version of the paper is submitted to the proceedings editor, in the prescribed format, by **01 June 2021** for the review by the Session Chair;
- The final (revised) version of the paper is submitted to the proceedings editor, addressing all issues raised by the Session Chair, by **15 July 2021**;
- At least one author has registered as a Congress delegate by 15 July 2021.

5. Contact Author Email Address

The contact author email address should appear explicitly in this section to facilitate future contacts. For example, mailto: corresponding@author.com

6. Copyright Statement

The authors confirm that they, and/or their company or organization, hold copyright on all of the original material included in this paper. The authors also confirm that they have obtained permission, from the copyright holder of any third party material included in this paper, to publish it as part of their paper. The authors confirm that they give permission, or have obtained permission from the copyright holder of this paper, for the publication and distribution of this paper as part of the ICAS proceedings or as individual off-prints from the proceedings.